CFD Simulations of Superorbital Reentry for a Phobos Sample Return Capsule

Marta Fernandes Pereira Bruxelas
marta.bruxelas@tecnico.ulisboa.pt

Instituto Superior Técnico, Universidade de Lisboa, Portugal

November 2017

Abstract

A simulation of the reentry flow for a Phobos Sample Return Mission is presented. The initial reentry velocity considered is 11.6 km/s and the capsule has the same forward body geometry as the Hayabusa capsule. The simulations are performed using CFD code SPARK, developed and maintained at IPFN. The heat fluxes along the capsule surface are analysed for several trajectory points, centered in the convective heating peak trajectory point, since the assessment of the total heat fluxes is paramount for the proper design of a TPS. A mesh generation process and mesh convergence study are presented. Two methods for calculating the transport properties, Wilke and Gupta-Yos, are applied and compared. The obtained results are also compared against a previous simulation performed using the same software considering the RAM-C II capsule reentry at 7.65 km/s. For the highest reentry speed, both models diverge more than for the lowest speed. An analysis of thermal nonequilibrium is performed applying Park's two-temperature model to account for thermal nonequilibrium and compared against thermal equilibrium conditions. Two trajectories for the capsule descent are considered in the scope of project DIVER, a steep and a shallow entry. The stagnation point convective heat flux is analysed at six key points for each trajectory and compared to the Sutton-Graves semi-empirical correlation used in the preliminary design.

Keywords: Reentry, Hypersonic, Aerothermodynamics, Convective Heat Fluxes

1. Introduction

Robotic planetary exploration missions rank among the most challenging endeavours in Space engineering. The Phobos Sample Return Mission was designed to collect samples from the Martian moon Phobos and returning them to Earth. One of this mission's most critical technologies is the one behind the superorbital Earth reentry originating from Mars/Phobos. During Earth reentry, the spacecraft is moving at velocities ranging from 13 to 6 km/s, crossing several hypersonic flow conditions. These velocities lead to the formation of a strong and high-temperature bow shock around the capsule. Because of the high temperature nature of this shock, the heat fluxes that reach the surface of the capsule will exceed what the surface material can withstand. Consequently, the proper selection of a Thermal Protection System (TPS) is very important when designing a reentry capsule. To this effect, an accurate assessment of wall heat fluxes during the high speed, hyperbolic reentry is therefore critical. These heat fluxes can be divided into two types, convective heating and radiative heating. Convective heating refers to the combined effect of the convective heat flux and the conduction heat flux. The radiative heat flux is sourced in the radiation emitted by the ionized flow.

DIVER (Desenho Integrado de VEículo de Reentrada) is a Portuguese consortium project comprising Spin.works, INEGI, IST-DEM and IPFN (Instituto de Plasmas e Fusão Nuclear), funded by Portugal2020. It gathers all the concurrent engineering required in the preliminary design of a reentry vehicle in the Phobos Sample Return mission and aims at demonstrating the national expertise on interplanetary exploration missions design. Two trajectories for the capsule descent are considered, one with a flight path angle (fpa) of -15.9°, Trajectory 15.9, and the other with fpa = -24.2°, Trajectory 24.2. In both trajectories, the maximum value of the reentry velocity is 11.6 km/s.

The purpose of this work is to 1) identify the key trajectory points for the proper design of the capsule; 2) calculate the convective heat fluxes for each trajectory key points; 3) compare the stagnation heat fluxes against correlation values; and 4) provide a first estimate of the heat fluxes for the next phase of the design. In order to accomplish these objectives, CFD simulations will be performed using the in-house IPFN CFD code SPARK (Software Package for Aerodynamics, Radiation and Kinetics) [1]. It is a multidimensional, second-order finite volume method discretization solver for Navier-Stokes and reactive flow governing equations in structured meshes. The simulations will consider two different transport models (Wilke and Gupta-Yos). These transport models have been previously implemented and discussed in the scope of a previous Master's thesis [2] and will be briefly summarized here. A one-temperature model and a multi-temperature model will be considered to account for thermal equilibrium and nonequilibrium conditions.

There are three approaches to study the reentry flowfield around a capsule: flight testing, ground testing and numerical simulations. The latter is the most economical and viable way of simulating reentry conditions. Nevertheless, this kind of simulations are challenging, especially the full capture of the multi-physics phenomena. As explained before, the gas is highly reactive in the shock layer owing to the large post-shock temperatures. To accurately model a hypersonic reentry flow, a large number of complex gas dynamics processes must be taken into account, such as molecular collisions leading to dissociation/recombination and/or ionization of molecules and/or atoms, charged particle interactions, and radiation [3]. The physical models that have been developed based on theory and experimental data are implemented in a computational solver that will perform numerical simulations with purpose of validating those models. Many numerical simulations have been performed for missions at superorbital velocities[1], such as the Stardust mission [4] [5], the Hayabusa mission [6], the FIRE II mission [1] [7] and the Apollo missions [8]. Not all numerical data obtained agreed well with either experimental data or flight data. This leads to the conclusion that despite the proved success of some models and correlations in properly defining the processes at reentry, there are still opportunities for further development in this area.

2. Governing Equations and Physical Models

During a superorbital reentry, the flow is characterized as a thermal nonequilibrium reacting flow. Consequently, it has to be defined by a multi-component model, which means the gas is treated as a mixture of individual chemical species, mixed in a single phase. Since the gas is not in chemical equilibrium, a chemical-kinetic model needs to be applied to model the gas composition.

During reentry the large amount of coherent kinetic energy in the hypersonic freestream is converted into translational energy of the gas across the strong bow shock wave. This energy is then transferred to the molecules' internal modes through further collision processes. There are four main thermal energy modes[2] translational energy, rotational energy, vibrational energy and electronic excitation energy [9]. In thermal equilibrium, every species thermal energy is associated to the same characteristic temperature $T = T_{\text{tra}} = T_{\text{rot}} = T_{\text{vib}} = T_{\text{exc}}$. However, usually species thermal energy modes are excited differently and thus, multiple temperatures must be considered. This thermal nonequilibrium is taken into account through the use of a multi-temperature model.

Equations (1 - 4) present the conservative equations for a thermal nonequilibrium reacting flow.

$$\frac{\partial(\rho c_i)}{\partial t} + \vec{\nabla} \cdot (\rho c_i \vec{u}) = \vec{\nabla} \cdot \vec{J}_i + \dot{\omega}_i \tag{1}$$

$$\frac{\partial(\rho \vec{u})}{\partial t} + \vec{\nabla} \cdot (\rho \vec{u} \otimes \vec{u}) = \vec{\nabla} \cdot [\tau] - \vec{\nabla} p \tag{2}$$

$$\frac{\partial(\rho E)}{\partial t} + \vec{\nabla} \cdot (\rho E \vec{u}) = \vec{\nabla} \cdot \left(\sum_k \vec{q}_{C_k} + \sum_i \vec{J}_i h_i + \vec{u} \cdot [\tau] - p\vec{u} \right) \tag{3}$$

$$\frac{\partial}{\partial t}(\rho \varepsilon_k) + \vec{\nabla} \cdot (\rho \vec{u} h_k) = \vec{\nabla} \cdot \left(q_{\vec{C_k}} + \sum_i \vec{J}_i h_{i,k} \right) + \dot{\Omega}_k \tag{4}$$

where ρ is the density, $\vec{u}$ the mean velocity in vectorial form, c_i the species i mass fraction, $\vec{J}_i$ the species i mass diffusion flux, $\dot{\omega}_i$ the species i source term, $[\tau]$ the viscous stress tensor, p the pressure, E the total energy, $\vec{q}_{C_k}$ the conduction heat flux, h the enthalpy of the flow, ε_k the thermal energy associated to each thermal energy mode and $\dot{\Omega}_k$ the thermal energy source term.

2.1. Kinetic Model

In the above stated equation for the species continuity (eq. 1), $\dot{\omega}_i$ is the species source term that accounts for the destruction and production of species. It is determined by the chemical-kinetic model. Depending on the kinetic scheme considered, the number of chemical reactions and their respective rates are different. The kinetic scheme considered in the present work is the 11-species air model developed by Park [10]. It considers the species O_2, N_2, NO, N, O, N_2^+, O_2^+, NO^+, N^+, O^+, e^-.

2.2. Multi-Temperature Model

The two-temperature model by Park[11] is implemented in SPARK. It assumes that the translational energy of the atoms and molecules and the rotational energy of the molecules are characterized by the same temperature T_{tra} and that T_{vib} characterizes the vibrational energy of the molecules, translational energy of the electrons and electronic excitation energy of atoms and molecules.

---

[1] These correspond to velocities above the escape velocity from Earth's gravity.

[2] Assuming the Born-Oppenheimer approximation.

2.3. Transport Models

The phenomena that take place during reentry lead to larger changes in the gas mixture transport properties. Consequently, an adequate model needs to be implemented. In the equations previously stated (eqs. 1 - 4), $\vec{J}_i$, $[\tau]$ and $\vec{q}_{C_k}$ define the dissipative fluxes. In the present work, the mass diffusion flux $\vec{J}_i$ is modelled by Fick's Law of diffusion:

$$\vec{J}_i = \rho D_i \vec{\nabla}(c_i) \tag{5}$$

where D_i represents the ith species mass diffusion coefficient. Moreover, it is considered that the viscous stress tensor $[\tau]$ assumes a Newtonian fluid and the Stokes hypothesis for the normal stresses:

$$[\tau] = \mu\left(\vec{\nabla}\vec{u} + (\vec{\nabla}\vec{u})^T\right) - \frac{3}{2}\mu(\vec{\nabla}\cdot\vec{u})[I] \tag{6}$$

where μ is the viscosity coefficient. Furthermore, the conduction heat flux in each energy mode, $\vec{q}_{C_k}$, is assumed to be given by Fourier's Law of heat conduction:

$$\vec{q}_{C_k} = \lambda_k \vec{\nabla} T_k \tag{7}$$

The most effective way of determining these properties is by applying approximate mixing rules, which are simplified forms of the Chapman-Enskog solution [12]. In this work, two different mixing rules are applied, the Wilke/Blottner/Eucken model and the Gupta-Yos/Collision Cross-Section model.

2.3.1 Wilke/Blottner/Eucken Model

Wilke's Model [13] for gas mixture viscosities was developed through the application of kinetic theory to the first order Chapman-Enskog relation. It assumes that all interactions between any particles present the same (hard sphere) cross-section [14]. The gas mixture viscosity μ and the thermal conductivity λ_k for each gas temperature are determined as follows:

$$\mu_m = \sum_{i=1}^{NS} \frac{x_i \mu_i}{\phi_i} \qquad \lambda_k = \sum_{i}^{NS} \frac{x_i \lambda_{k,i}}{\phi_i} \tag{8}$$

where x_i is the species molar fraction and μ_i represents the individual viscosities. ϕ_i is a scale factor given by:

$$\phi_i = \sum_{j=1}^{NS} \left[1 + \sqrt{\frac{\mu_i}{\mu_j}}\left(\frac{M_j}{M_i}\right)^{\frac{1}{4}}\right]^2 \Bigg/ \sqrt{8\left(1 + \frac{M_j}{M_i}\right)} \tag{9}$$

where M_* represents each species' (i's or f's) molar mass.

For the species viscosities, curve fits determined by Blottner [15] are considered:

$$\mu_i(T_{\mathrm{tra,i}}) = 0.1\exp((A_i \ln T_{\mathrm{tra,i}} + B_i)\ln T_{\mathrm{tra,i}} + C_i) \tag{10}$$

where A_i, B_i and C_i are curve fitted coefficients for each species.

Eucken's relation [16] is used to determine each species thermal conductivity:

$$\lambda_{\mathrm{tra},i} = \frac{5}{2}\mu_i C_{V_{\mathrm{tra},i}} \qquad \lambda_{k\neq\mathrm{tra},i} = \mu_i C_{V_{k,i}} \tag{11}$$

where $C_{V_{k,i}}$ represents the specific heat at a constant volume of the i species in each energy mode. In thermal nonequilibrium, the contributions of each species should be accounted for differently in the mixing rule, according to the multi-temperature model considered.

The species mass diffusion coefficient is given by a single binary coefficient D assuming a constant Lewis number, $\mathrm{Le} = 1.2$:

$$D_i = D = \frac{\mathrm{Le}\lambda}{\rho C_P} \tag{12}$$

where C_P is the gas mixture total specific heat at a constant pressure and λ represents the total thermal conductivity of the gas mixture. The Lewis number Le corresponds to the ratio of the energy transport due to mass diffusion relative to the one due to thermal conduction.

2.3.2 Gupta-Yos/Collision Cross-Section Model

Another method to calculate the transport properties of a gas mixture is by using the Gupta-Yos model [17], a simplification of the Chapman-Enskog solution. The main difference between the Wilke and the Gupta-Yos models is that the latter considers each collision's corresponding cross-section. Consequently, it is assumed to be more accurate because the true nature of the viscosity collision integrals is taken into account. The collision integrals are defined as follows:

$$\Delta_{ij}{}^{(1)}(T_c) = \tfrac{8}{3}\left[\tfrac{2M_iM_j}{\pi RT(M_i+M_j)}\right]^{1/2} \pi\overline{\Omega}_{ij}{}^{(1,1)} \tag{13}$$

$$\Delta_{ij}{}^{(2)}(T_c) = \tfrac{16}{5}\left[\tfrac{2M_iM_j}{\pi RT(M_i+M_j)}\right]^{1/2} \pi\overline{\Omega}_{ij}{}^{(2,2)} \tag{14}$$

where $\overline{\Omega}_{ij}{}^{(1,1)}$ and $\overline{\Omega}_{ij}{}^{(2,2)}$ represent weighted averages of the cross-sections. These collision integrals are a function of the controlling temperature T_c that varies depending on the type of particles colliding. For collisions between heavy-particles, the controlling temperature is the translational/rotational temperature (T_{tra}), whereas the one for collisions involving electrons is the vibrational/electron/electronic excitation temperature (T_{vib}) [5].

For the calculation of the gas mixture viscosity, the mixing rule is used:

$$\mu^{(1)} = \sum_i^{NS} \frac{m_i x_i}{\sum\limits_j^{NS} x_j \Delta_{ij}^{(2)}} \tag{15}$$

where m_i is the ith species mass. The translational mode of heavy species λ_{tra} reads:

$$\lambda_{\text{tra}} = \frac{15}{4} k_B \sum_i \frac{x_i}{\sum_j \alpha_{i,j} x_j \Delta_{ij}^{(2)}} \tag{16}$$

and the translational mode of electrons λ_{e} is:

$$\lambda_{\text{e}} = \frac{15}{4} k_B \frac{x_e}{\sum\limits_j \alpha_{e,j} x_j \Delta_{ej}^{(2)}} \tag{17}$$

where k_B is the Boltzmann constant and $\alpha_{i,j}$ is given by:

$$\alpha_{i,j} = 1 + \frac{[1 - M_i/M_j][0.45 - 2.54(M_i/M_j)]}{[1 + (M_i/M_j)]^2} \tag{18}$$

The global thermal conductivities associated with the rest of the heavy species energy modes, λ_{rot}, λ_{vib}, λ_{exc} are:

$$\lambda_{\text{rot}} = \sum_i \frac{x_i m_i C_{V_{\text{rot},i}}}{\sum\limits_j^{NS} x_j \Delta_{ij}^{(1)}} \tag{19}$$

$$\lambda_{\text{vib}} = \sum_i \frac{x_i m_i C_{V_{\text{vib},i}}}{\sum\limits_j^{NS} x_j \Delta_{ij}^{(1)}} \tag{20}$$

$$\lambda_{\text{exc}} = \sum_i \frac{x_i m_i C_{V_{\text{exc},i}}}{\sum\limits_j^{NS} x_j \Delta_{ij}^{(1)}} \tag{21}$$

In thermal equilibrium, the total thermal conductivity λ is given by:

$$\lambda = \lambda_{\text{tra}} + \lambda_{\text{e}} + \lambda_{\text{rot}} + \lambda_{\text{vib}} + \lambda_{\text{exc}} \tag{22}$$

In thermal nonequilibrium, the thermal conductivity associated with each temperature mode is calculated by considering the individual contributions of each species according to the multi-temperature model considered, where the global temperature parameter T is replaced by the appropriate mode temperature.

The mass diffusion coefficient D_{ij} defines the diffusion velocity of each species relative to the other species and reads:

$$D_{ij} = \frac{k_B T_c}{p \Delta_{ij}^{(1)}} \tag{23}$$

An average of the diffusion coefficient relative to the remaining gas mixture D_i is determined by:

$$D_i = \frac{1 - x_i}{\sum\limits_{j \neq i} \frac{x_j}{D_{ij}}} \tag{24}$$

2.3.3 Ambipolar Diffusion

In an ionized gas, each charged particle induces an electric field, which influences the other particles motion. This results in an increase in the diffusion of the ions, which are *pulled* by the more mobile electrons, which in turn are slowed down by the heavier ions. The two species finally diffuse with the same velocity, mainly imposed by the heavier species. Since the electro-static forces are not considered in the conservation equations, this phenomena can only be taken into account by artificially introducing this effect in the calculation of the charged particles diffusion. The ambipolar corrections account for this increase in diffusion velocity of ions and decrease in velocity of electrons due to the electrostatic interactions between the two.

For ions, Chen [18] shows that the ambipolar diffusion coefficient is given by:

$$D_{\text{ion}}^a = \big(1 + \frac{T_{\text{e}}}{T_{\text{ion}}}\big) D_{\text{ion}} \tag{25}$$

where D_{ion} is the ion free diffusion coefficient and T_{e} and T_{ion} are the translational temperatures of the electrons and the ions, respectively. In thermal equilibirum, this ionic factor is simply equal to 2 ($D_{\text{ion}}^a = 2D_{\text{ion}}$), assuming that all heavy species are in equilibrium with a common translational temperature.

For electrons, the ambipolar diffusion coefficient is defined as [19]:

$$D_{\text{e}}^a = M_{\text{e}} \frac{\sum_{i=ion} D_i^a x_i}{\sum_{i=ion} M_i x_i} \tag{26}$$

This is only valid if all the ions have the same free diffusion velocity and electrical mobility.

3. Numerical Setup

After correctly defining the problem, the conditions in which the simulations will be performed need to be established.

3.1. Selection of the Key Trajectory Points

This works' role in the DIVER project is to calculate the heat fluxes present at the wall so that a suitable TPS can be designed. Two separate trajectories were considered and for each of these trajectories, semi-empirical correlations were applied as a first approach, such as it is customary when testing a large number of possible flight profiles and geometries, where full CFD simulations are impractical.

For the convective heating, the Sutton-Graves equation [20] was applied. To analyse radiative heating, the expression developed by Tauber and Sutton[21] was considered. Both assume chemical equilibrium flow. Figure 1 shows the results obtained by Spin.works for the convective (dark blue line) and radiative (light blue line) heat fluxes, the

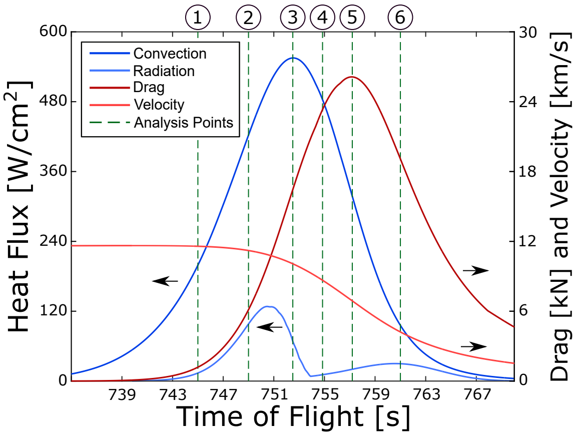

(a) Trajectory 15.9

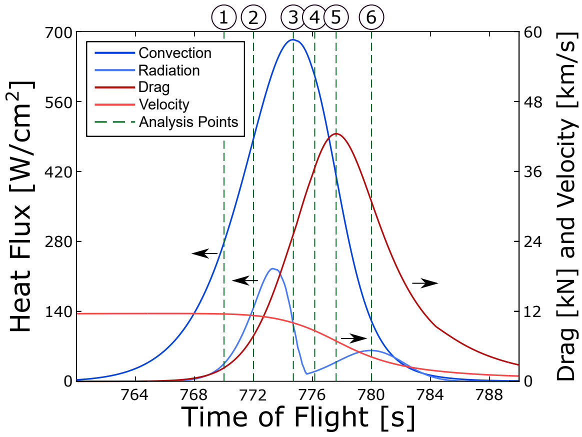

(b) Trajectory 24.2

Figure 1: Results for the semi-empirical correlations for both trajectories.

drag (dark red line) and velocity (light red line) distributions during reentry and the points where the analysis will be performed (green dashed line) for (a) Trajectory 15.9 and (b) Trajectory 24.2.

Six key points per trajectory were selected to perform CFD simulations. Point 1, 2, 4 and 6 were selected to properly compare the CFD results with the correlations used. Point 3 represents the convective heating peak, it is the most critical point in each trajectory. Point 5 corresponds to the peak in drag, it is the point where the mechanical loads are the highest. Tables 1 and 2 show the selected points data for Trajectory 15.9 and Trajectory 24.2, respectively. The data was calculated considering the US Standard Atmosphere 1976 to model Earth's Atmospheric profile as a function of altitude.

3.2. Mesh Generation

A mesh generation study was performed considering the initial conditions for the peak heating (point 3) of Trajectory 15.9. Figure 2 shows the capsule geometry where the forward body is highlighted in the drawing. The body is axisymmetric and therefore, only half of the front body will be considered in the computational domain, since a 0° angle of attack is also assumed.

Table 1: Points where the analysis will be performed for Trajectory 15.9.

	Trajectory 15.9		
	Velocity [km/s]	Density [g/m^3]	Temperature [K]
Point 1	11.58	0.024	202.03
Point 2	11.21	0.141	230.24
Point 3	10.07	0.486	257.18
Point 4	8.63	0.964	270.65
Point 5	6.89	1.726	266.79
Point 6	4.22	3.599	252.34

Table 2: Points where the analysis will be performed for Trajectory 24.2.

	Trajectory 24.2		
	Velocity [km/s]	Density [g/m^3]	Temperature [K]
Point 1	11.56	0.048	210.86
Point 2	11.29	0.178	235.07
Point 3	10.02	0.758	267.56
Point 4	8.73	1.451	270.32
Point 5	6.92	2.776	257.35
Point 6	4.18	5.888	243.10

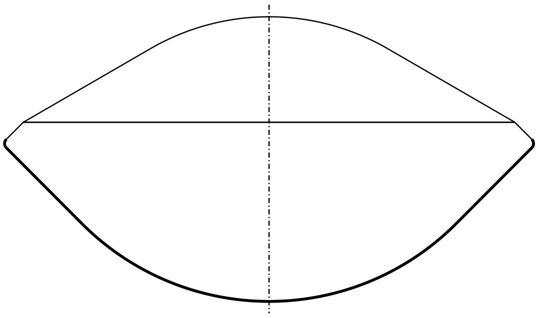

Figure 2: DIVER capsule geometry.

At the end of the mesh generation process, a final mesh configuration was selected. Afterwards, a mesh convergence exercise was performed, to obtain the best results at the least computational effort. Figure 3 shows a comparative analysis of (a) the temperature profiles along the stagnation line and (b) the wall heat fluxes for three mesh resolutions. Ni refers to the number of mesh cells along the stagnation line.

Analysing Fig. 3 it can be seen that Ni = 90 (red line) and Ni = 120 (black line), present closer results than Ni = 45 (blue line). Consequenty, it was considered the latter mesh is too rough for the desired simulations. Because the heat flux profiles obtained for Ni = 120 are still 16% higher than for Ni = 90, it was concluded that the most suitable

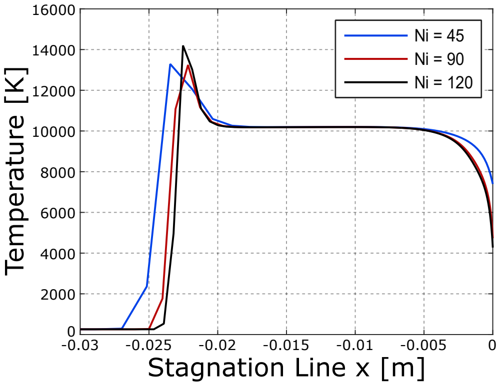

(a) Stagnation Line Temperature

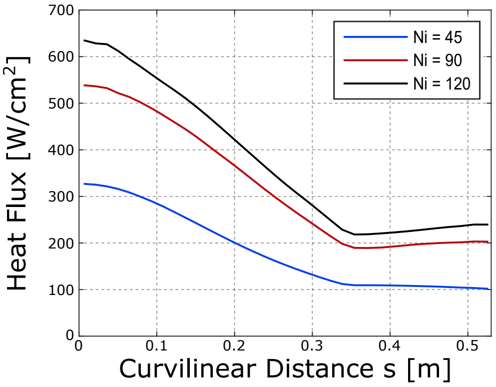

(b) Wall Heat Flux

Figure 3: Stagnation Line Temperature (a) and Wall Heat Flux (b) profiles for three different values of Ni, where Ni is the number of mesh cells along the stagnation line.

mesh for the simulations is the one where Ni = 120. More refined meshes were tested, however these did not manage to converge to a realistic flow profile. Figure 4 shows the final mesh. The mesh is refined near the wall to account for the boundary layer.

3.3. Initial and Boundary Conditions

The initial conditions for each trajectory point are detailed in tables 1 and 2. Figure 4 shows the mesh and the boundary conditions considered in the simulations performed in this work.

In addition to the boundary conditions previously stated, a condition will be considered to account for how the flow interacts with the surface. A fully catalytic wall boundary condition is applied, assuming that all atoms/electron-ion pairs which collide with the surface recombine into molecules/neutral species. It represents a pessimistic limit for the overall heat flux (since these catalytic reactions are exothermal).

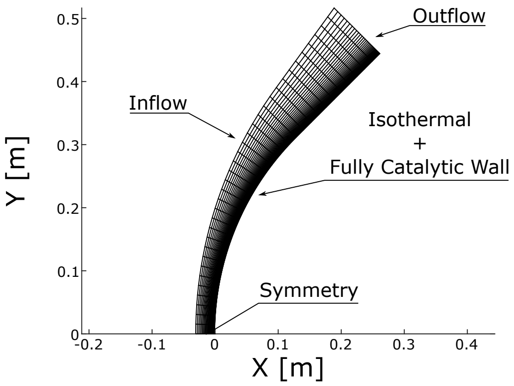

Figure 4: Boundary conditions considered for the CFD domain.

4. Results

4.1. Impact of Transport Model and Velocity

The following analysis was performed on point 3 of Trajectory 15.9. The results obtained were compared considering two transport models, Wilke and Gupta-Yos. The impact of the velocity was studied by comparing the results obtained in the present work to those obtained by Loureiro [2]. Both simulations were performed on SPARK and considered the same kinetic scheme and thermal equilibrium. In the simulations ran by Loureiro the RAM-C II capsule geometry and a reentry velocity of 7.65 km/s were considered.

Figure 5 shows the stagnation line temperature profiles for both mixing rules, at reentry speeds of 10 km/s (a) and 7.65 km/s (b).

Focusing on the results obtained in the present work (Fig. 5a), it can be seen that the greatest discrepancy in the results obtained for each transport model lies in the boundary layer. Around x = -0.0025 m, the Gupta-Yos model (black line) shows a steeper decrease in temperature when compared to the Wilke model (red line). Moreover, the Gupta-Yos model predicts a peak temperature 7% higher than the Wilke model.

Comparing the results obtained for each reentry velocity, there are two main differences. 1) The results agree better at lower velocities. This will be addressed later on at the end of this section; and 2) for the lowest velocity, there is no region where a quasi steady state flow is achieved between the shock wave and the boundary layer. The reason for the absence of this region is that the chemical reactions, in the shock region, occur at a slower rate, when compared to the highest velocity. One would expect the temperature peak value corresponding to the highest velocity to be much higher. However, due to the roughness of the mesh in this area considered in the present work, the shock peak is not fully captured and therefore, the peak temperature

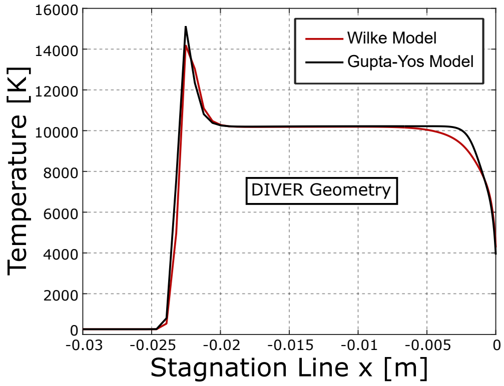

(a) 10 km/s

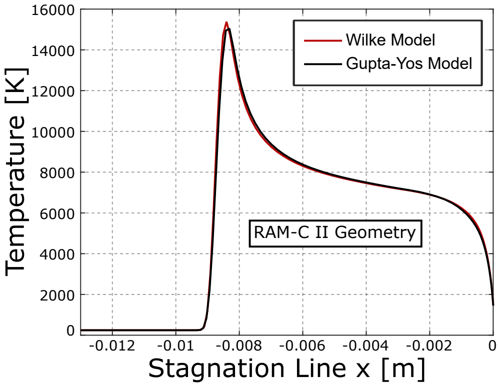

(b) 7.65 km/s

Figure 5: Stagnation line temperature profiles for both mixing rules, for a reentry speed of 10 km/s (a) and 7.65 km/s (b).

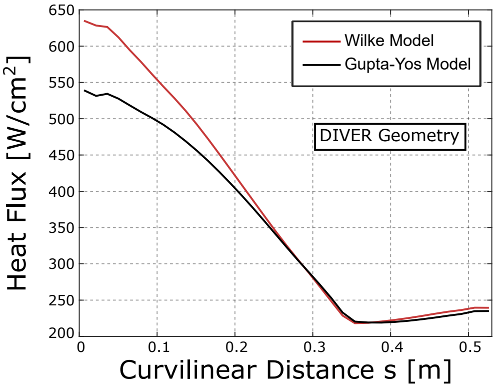

(a) 10 km/s

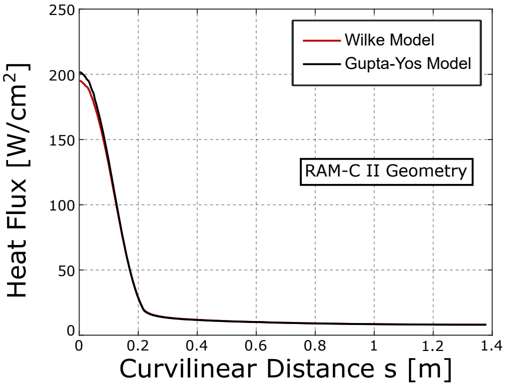

(b) 7.65 km/s

Figure 6: Wall Heat Flux profiles for both mixing rules, for a reentry speed of 10 km/s (a) and 7.65 km/s (b).

appears similar in both cases.

Figure 6 shows the wall heat flux profiles for both transport models, for a reentry speed of 10 km/s (a) and 7.65 km/s (b).

Focusing on the results performed at 10 km/s (Fig. 6a), there is a great difference in the wall heat flux profiles depending on the selected transport model. The peak heat flux obtained is 640 W/cm^2 for the Wilke model, 19% higher than for the Gupta-Yos model. It can be seen that for both curves, there is a slight disturbance around $s = 0.04$ m, which is currently attributed to numerical errors. A possible cause for this is the carbuncle problem [22]. It is defined as a local displacement of the bow shock wave shape near the stagnation line, which compromises the accuracy of the heat transfer predictions made by numerical simulations of hypersonic flows.

Comparing the results for both reentry velocities, the heat fluxes at the wall are about three times higher for 10 km/s, which agrees well with the increased temperature gradient at the surface.

Analysing Figs. 5 and 6, the results obtained for both transport models agree better at the lowest velocity. This is related to the increase in the degree of ionization of the flow at higher velocities, because these models were formulated assuming a weakly ionized gas.

4.2. Impact of Multi-Temperature Model

As discussed in section 2.2, Park's two-temperature model is implemented in SPARK to account for thermal nonequilibrium. Figure 7 shows profiles for (a) the stagnation line temperatures and (b) the wall heat flux for thermal nonequilibrium and thermal equilibrium. This simulation was performed on the same peak heating point for trajectory 15.9, point 3. A fully catalytic boundary condition at the surface and the Gupta-Yos transport model were considered.

Focusing on Fig. 7a, the translational/rotational temperature (red line) profile follows the same overall trend as the temperature profile considering thermal equilibrium (black line), although it does not stabilize. However, the peak in translational temperature reaches 22000 K, 27% higher than for the thermal equilibrium case. The

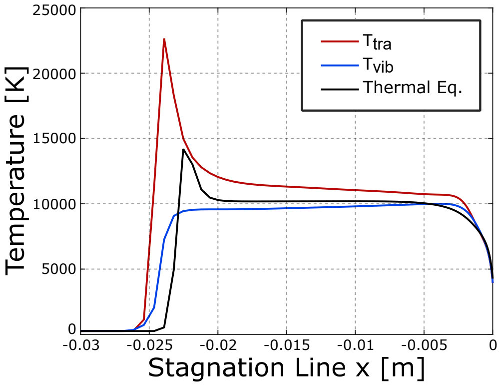

(a) Stagnation Line Temperatures

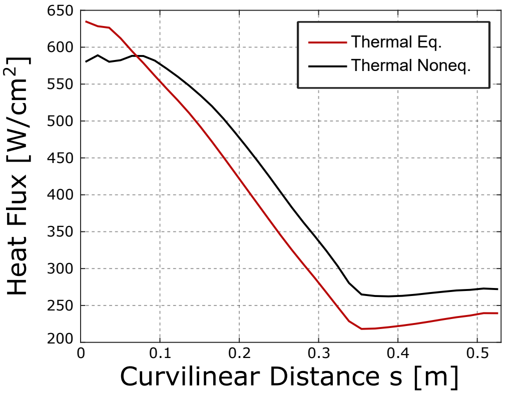

(b) Wall Heat Flux

Figure 7: Profiles for (a) the stagnation line temperatures (b) wall heat flux for thermal equilibrium and nonequilibrium.

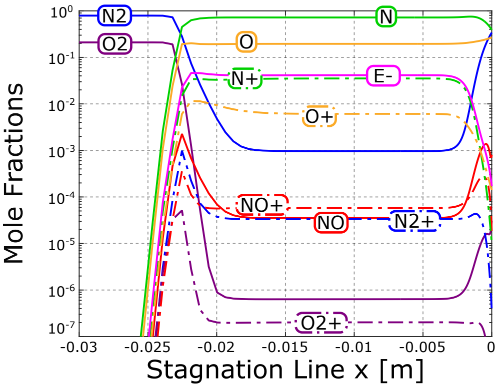

(a) Species Mole Fractions

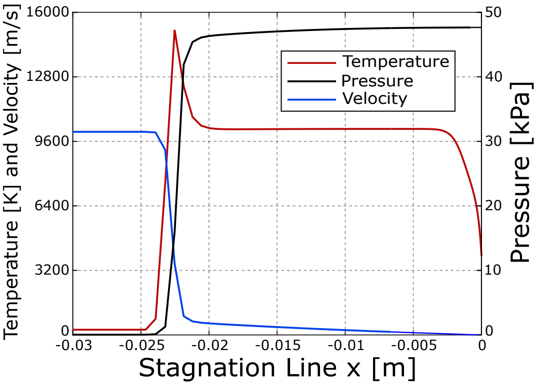

(b) Temperature Pressure Velocity

Figure 8: Stagnation line profiles for (a) species mole fractions and (b) temperature, pressure and velocity.

vibrational/electron/electronic excitation temperature (blue line) follows a more distinct profile. The discrepancy in the profiles for the translational/rotational temperature and the vibrational/electron/electronic excitation temperature leads to the conclusion that there is a very strong thermal nonequilibrium, as would be expected for the flow initial conditions. Thermal equilibrium is only reached in the boundary layer.

Figure 7b presents the wall heat flux results obtained for thermal equilibrium (red line) and thermal nonequilibrium (black line). Both present the same overall trend after s = 0.09 m. Before this point, both heat fluxes present a disturbance at s = 0.04 m, supporting the previous assumption of the carbuncle problem. The stagnation point heat flux predicted for the thermal nonequilibrium is approximately 580 W/cm^2, 9% lower than the one predicted for the thermal equilibrium case. It would be expected that the heat fluxes at the wall be the same along the capsule since thermal equilibrium is reached at the boundary layer. However, the temperature gradients differ, leading to slightly different heat fluxes. Nonetheless, the differences remain lower than 10% in the critical region of the stagnation streamline, allowing for the use of a more simplified and time-efficient single-temperature thermochemical model in the rest of the analysis.

4.3. Peak Heating Point Analysis

This analysis was performed for point 3 of Trajectory 15.9, a key point in the trajectory for the design of the TPS, since it corresponds to the peak in convective heating.

Figure 8 shows the results for (a) species mole fractions and (b) temperature, pressure and velocity profiles along the stagnation line.

Figure 8a shows that the mole fractions of N_2 and O_2 decrease after the bow shock (x = -0.022 m), whereas the rest of the species mole fractions increase after this point. Gas chemical composition stabilizes from x = -0.020 m up to x = -0.003 m (the quasi steady state region). Afterwards, concentrations of N_2, O_2 and NO increase due to the recombination reactions taking place near the capsule surface. This is balanced by the decrease in the molar fractions of species N_2^+, O_2^+, NO^+, e^- and N.

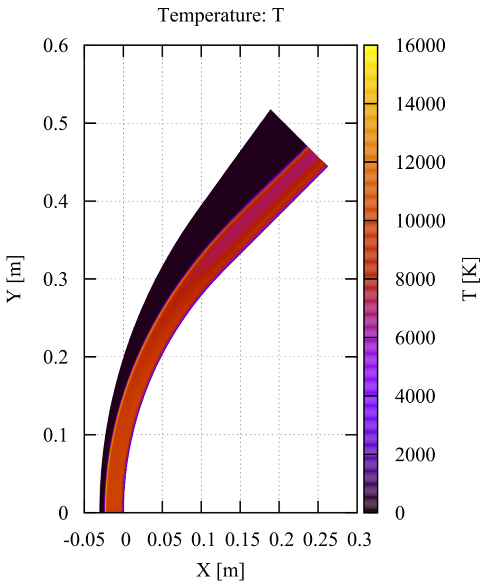

Figure 9: Temperature 2D field.

One would expect the molar fraction of O to decrease at the surface due to the recombination of O_2 ($O + O + \text{wall} \Rightarrow O_2$), however that is not the case, owing to the fact that this species is involved in more recombination reactions.

Focusing on Fig. 8b, for the shock peak (x = -0.022 m) there is an increase in temperature and pressure, whereas the velocity decreases. After reaching its peak, temperature decreases rapidly until it stabilizes at 10000 K, from x = -0.02 m up to x = -0.003 m. It then decreases abruptly until reaching the capsule surface at x = 0 m with the imposed wall temperature. Regarding the pressure, it rises until 47.7 kPa in the shock region, at x = -0.022 m, and remains stable until the capsule wall (x = 0 m). The velocity drops abruptly from 10000 to ≈ 960 m/s in the shock region and afterwards gradually decreases until V = 0 m/s at the capsule wall.

Figure 9 depicts the temperature 2D field. It shows the shock wave position very clearly due to the abrupt temperature rise. Towards the outflow boundary condition the temperatures in the shock layer are gradually lower (above Y = 0.3 m). This is due to the shock wave position relative to the flow. In the stagnation line, the shock wave is normal to the flow and the temperature gradient is very high. Moving along the shock wave, it becomes an oblique shock resulting in a lower temperature gradient.

4.4. Heat Fluxes for Project DIVER

For the key trajectory points detailed in section 3.1, CFD simulations were performed considering the Gupta-Yos transport model, thermal equilibrium and a fully catalytic wall, owing to the conclusions of previous sections. A comparison between the 6 selected points and the continuous correlated data-points for the two reentry trajectories has been carried out.

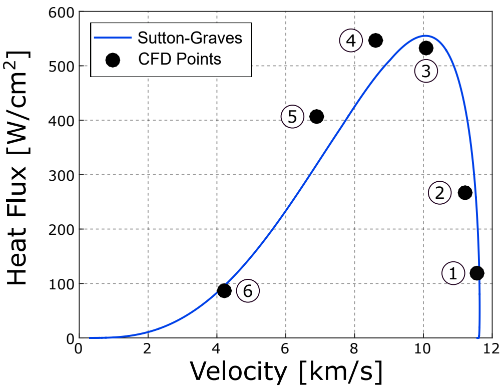

(a) Trajectory 15.9

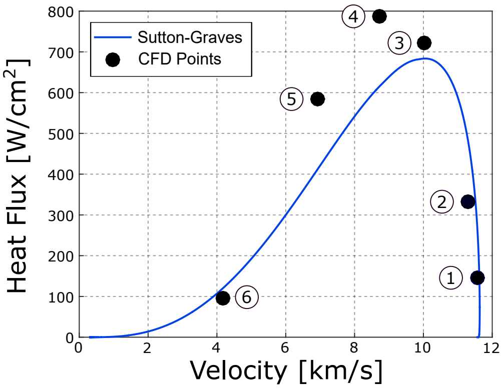

(b) Trajectory 24.2

Figure 10: Comparison of the data obtained in this work and the Sutton-Graves correlation for the convective heat flux along (a) Trajectory 15.9 and (b) Trajectory 24.2.

Figure 10 compares the data obtained in this work with the Sutton-Graves correlation for the convective heat flux along (a) Trajectory 15.9 and (b) Trajectory 24.2.

For both trajectories, some CFD points predict a slightly higher convective stagnation heat flux than the Sutton-Graves correlation. The highest discrepancy (48%) was found for Trajectory 24.2 in the point with the highest velocity, point 1. The peak heating point, for both trajectories is point 4, as opposed to number 3 in the correlation. The discrepancies found between the results are due to the fact that, as mentioned in section 3.1, the Sutton-Graves equation assumes chemical equilibrium. Overall CFD results correlate well with the semi-empirical results, providing confidence to the thermal protections system design process.

5. Conclusions

A successful comparison between the Wilke and the Gupta-Yos transport models was performed for an hyperbolic Earth reentry. It was found that for higher reentry velocities, the selection of the method to calculate transport properties influences the results more than for lower velocities, on account of the increased degree of ionization of the flow.

An analysis of the impact of applying a multi-temperature model was carried out. Park's two-temperature model was considered. It was concluded that the flow at these reentry conditions, at 10 km/s, presents a very strong thermal nonequilibrium, as would be expected. However, this does not significantly impact the overall aerothermodynamics of the flow due to the fact that the mole fractions of the molecules in the shock layer are very low and thus constitute a very small percentage of the flow composition. In this region, the ions and atoms characterize the flow and hence the vibrational temperature loses its meaning.

The trajectory point corresponding to the peak in convective heating was thoroughly analysed. The species molar fractions validated the assumption of a fully catalytic wall boundary condition.

The stagnation point convective heat flux was analysed for all the key trajectory points and compared to the Sutton-Graves correlation. The results agreed reasonably with the correlation. Discrepancies may be attributed to the fact that the correlation assumes that the flow is in chemical equilibrium.

Acknowledgements

I gratefully acknowledge the support of Prof. Mário Lino da Silva, Dr. Maria Castela, Prof. Paulo Gil, Dr. Bruno Lopez and company Spin.works for the success of the present work.

References

[1] B. Lopez and M. Lino da Silva. SPARK : A Software Package for Aerodynamics , Radiation and Kinetics. In *46th AIAA Thermophysics Conference*, 2016.

[2] D. D. Loureiro. High-Temperature Modeling of Transport Properties in Hypersonic Flows. Master's thesis, Instituto Superior Técnico, 2015.

[3] K. J. Higdon, D. B. Goldstein, and P. L. Varghese. Sensitivity Analysis of Direct Simulation Monte Carlo Parameters for Ionizing Hypersonic Flows. *Journal of Thermophysics and Heat Transfer*, 2017.

[4] K. A. Trumble, I. Cozmuta, S. Sepka, P. Jenniskens, and M. Winter. Postflight Aerothermal Analysis of the Stardust Sample Return Capsule. *Journal of Spacecraft and Rockets*, 2010.

[5] H. Alkandry, I. D. Boyd, and A. Martin. Comparison of Models for Mixture Transport Properties for Numerical Simulations of Ablative Heat-Shields. In *51st AIAA Aerospace Sciences Meeting Including the New Horizons Forum and Aerospace Exposition*, 2013.

[6] E. Fahy, R. J. Gollan, D. R. Buttsworth, P. A. Jacobs, and R. G. Morgan. Expansion Tube and Computational Fluid Dynamics Studies of Superorbital Earth Re-entry. In *46th AIAA Thermophysics Conference*, 2016.

[7] L. C. Scalabrin and I. D. Boyd. Numerical Simulations of the FIRE-II Convective and Radiative Heating Rates. In *39th AIAA Thermophysics Conference*, 2007.

[8] C. Park. Stagnation-Point Radiation for Apollo 4. *Journal of Thermophysics and Heat Transfer*, 2004.

[9] J. D. Jr. Anderson. *Hypersonic and High Temperature Gas Dynamics.* AIAA, 1989.

[10] C. Park, R. L. Jaffe, and H. Partridge. Chemical-Kinetic Parameters of Hyperbolic Earth Entry. *Journal of Thermophysics and Heat Transfer*, 2001.

[11] C. Park. Assessment of Two-Temperature Kinetic Model for Ionizing Air. *Journal of Thermophysics and Heat Transfer*, 1989.

[12] S. Chapman and T. G. Cowling. *The Mathematical Theory of Non-Uniform Gases.* Press Syndicate of the University of Cambridge, 1990.

[13] C. R. Wilke. A Viscosity Equation for Gas Mixtures. *The Journal of Chemical Physics*, 1950.

[14] G. E. Palmer and M. J. Wright. Comparison of Methods to Compute High-Temperature Gas Viscosity. *Journal of Thermophysics and Heat Transfer*, 2003.

[15] F. G. Blottner, M. Johnson, and M. Ellis. Chemically Reacting Viscous Flow Program for Multi-Component Gas Mixtures. Technical report, Sandia Laboratories, 1971.

[16] W. G. Vincenti and C. H. Kruger. *Introduction to Physical Gas Dynamics.* Krieger Publishing Company, 2002.

[17] P.A. Gnoffo, R. N. Gupta, and J. L. Shinn. Conservation Equations and Physical Models for Hypersonic Air Flows in Thermal and Chemical Nonequilibrium. Technical report, NASA, 1989.

[18] F. F. Chen. *Introduction To Plasma Physics and Controlled Fusion*, volume 1. Plenum Press, 1984.

[19] J. H. Lee. Basic Governing Equations for the Flight Regimes of Aeroassisted Orbital Transfer Vehicles. In *AIAA 19th Thermophysics Conference*, 1984.

[20] K. Sutton and R. A. Graves. A General Stagnation-Point Convective-Heating Equation for Arbitrary Gas Mixtures. Technical report, NASA, 1971.

[21] M. E. Tauber and K. Sutton. Stagnation-Point Radiative Heating Relations for Earth and Mars Entries. *Journal of Spacecraft and Rockets*, 1990.

[22] R. W. MacCormack. Carbuncle Computational Fluid Dynamics Problem for Blunt-Body Flows. *Journal of Aerospace Information Systems*, 2013.